

Figure 1.

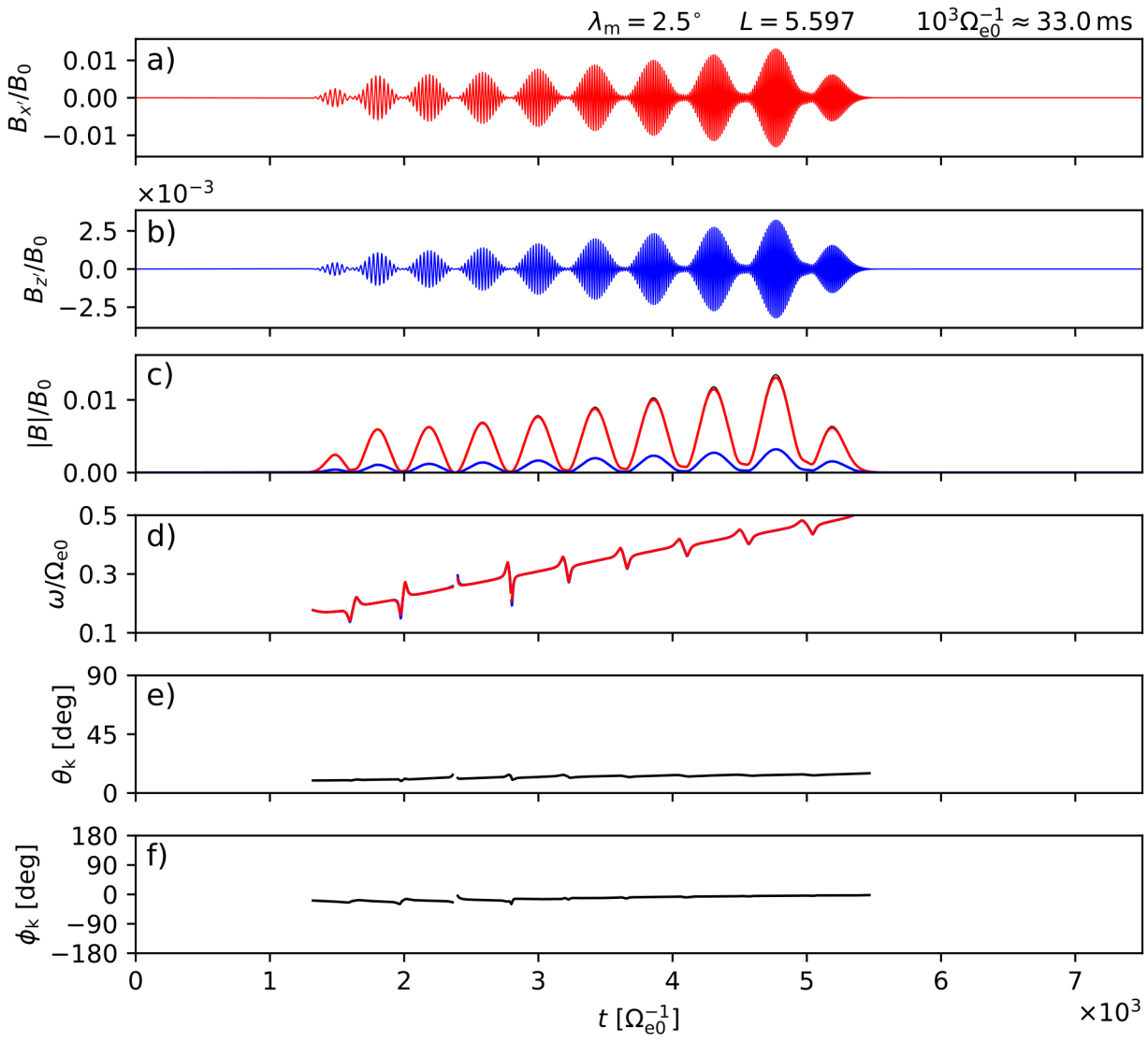


Figure 2.

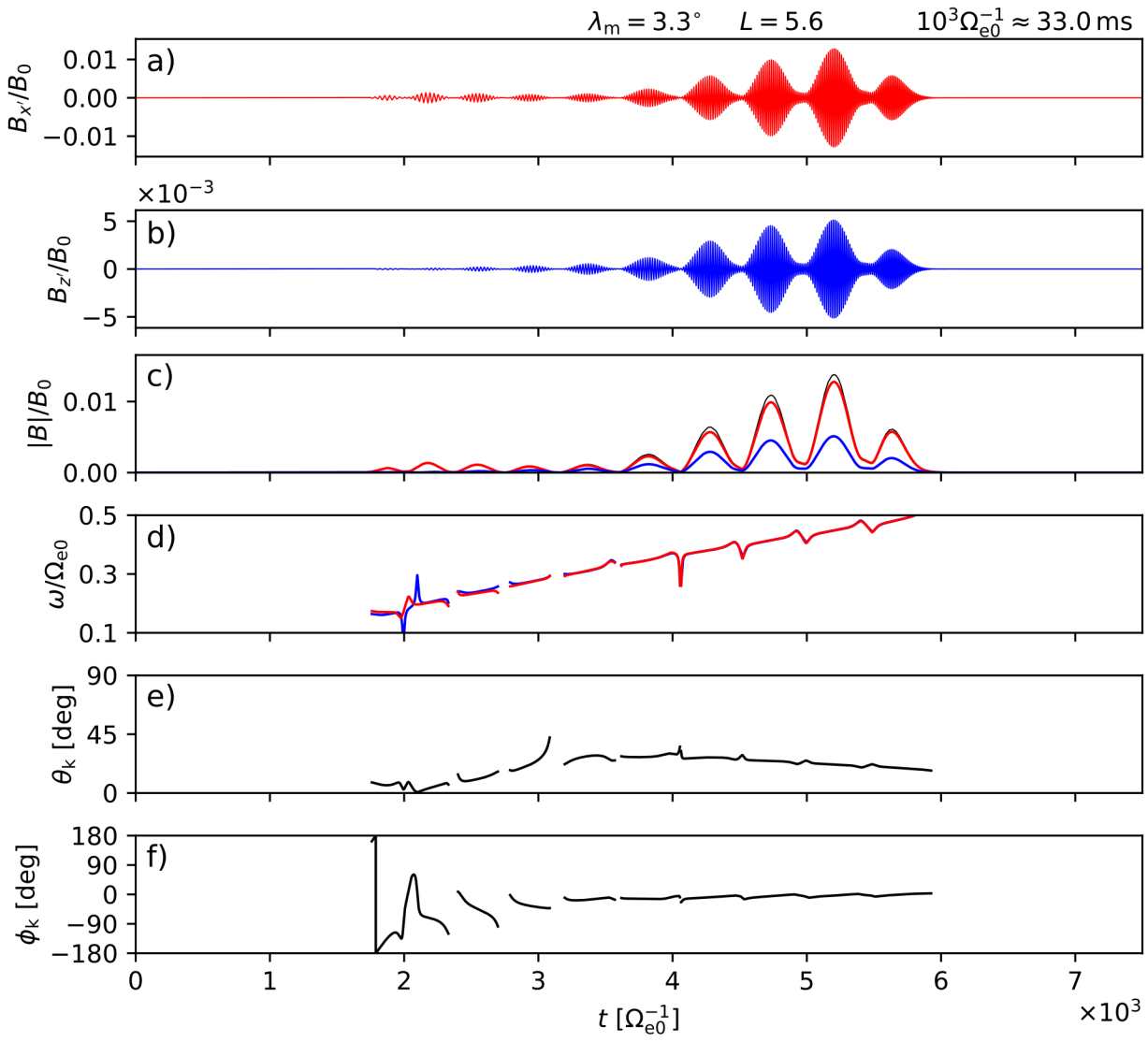


Figure 3.

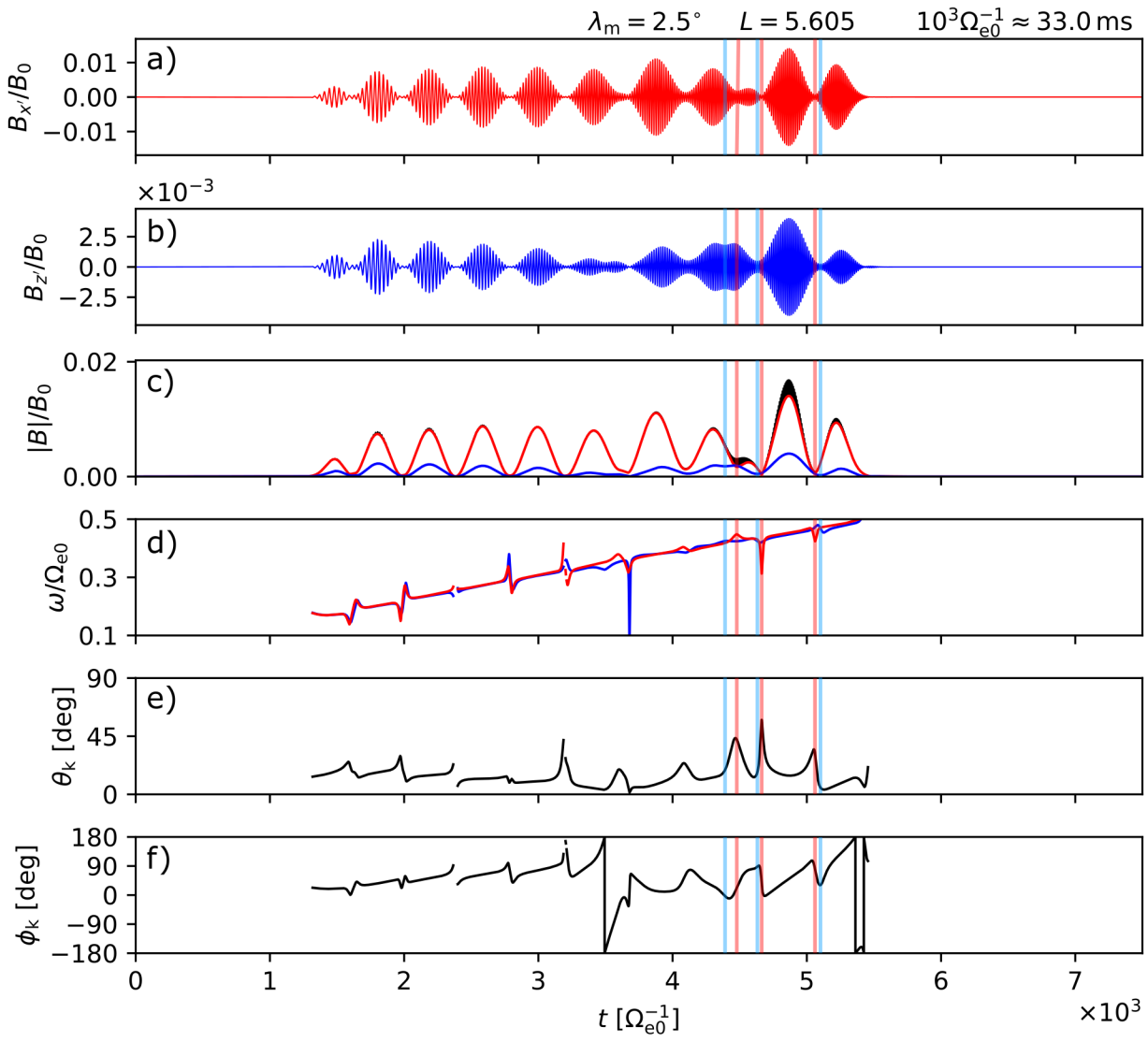
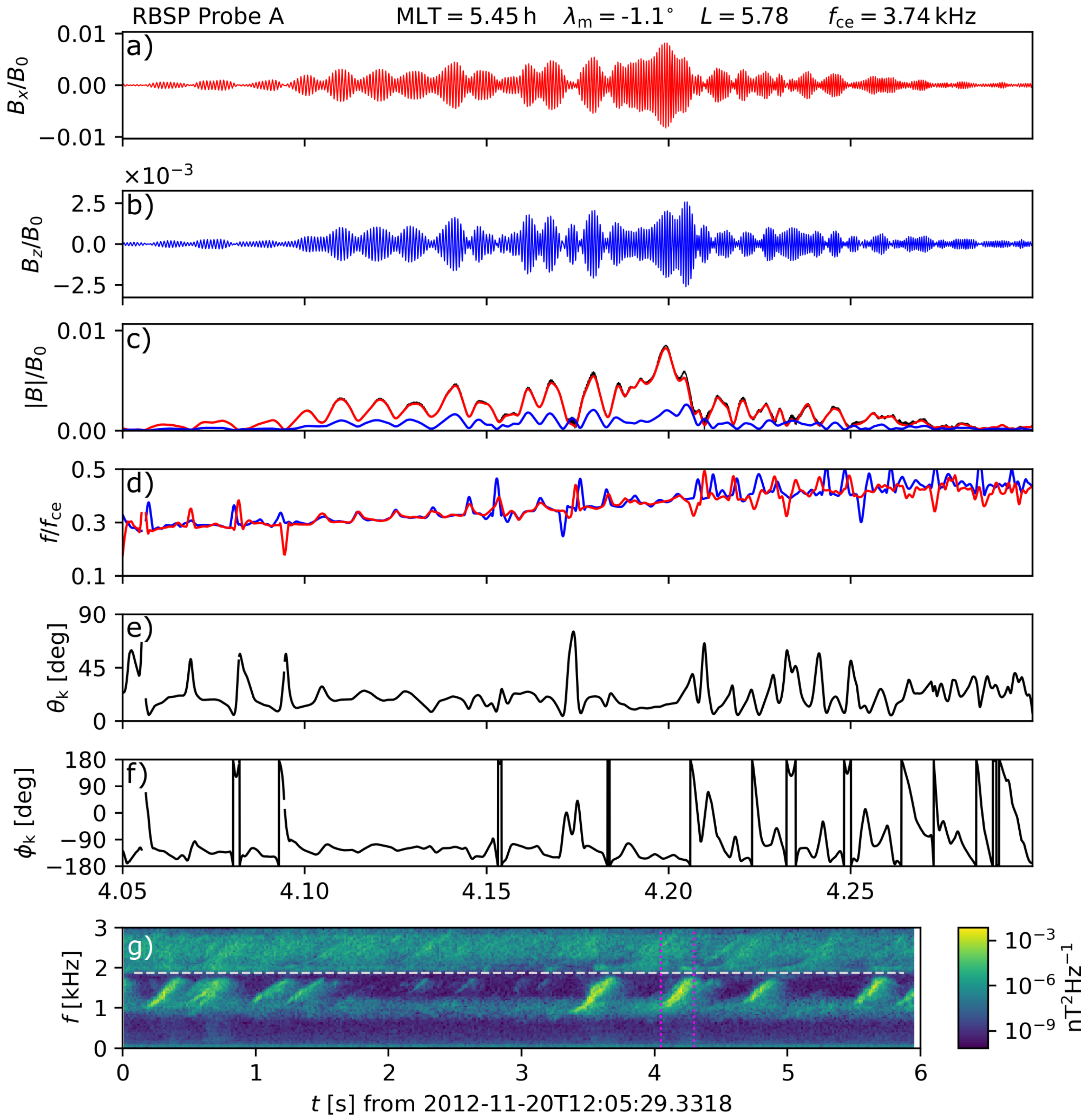


Figure 4.



Effects of Field-Aligned Cold Plasma Density Filaments on the Fine Structure of Chorus

M. Hanzelka^{1,2}, O. Santolík^{1,3}

¹Department of Space Physics, Institute of Atmospheric Physics, Czech Academy of Sciences, Prague,
Czech Republic

²Center for Space Physics, Boston University, Boston, Massachusetts, USA

³Faculty of Mathematics and Physics, Charles University, Prague, Czech Republic

Key Points:

- Propagation of lower-band chorus subpackets near their equatorial source is simulated with finite-difference time-domain methods
- Narrow, field-aligned density enhancement (ducts) create different amplitude modulations in parallel and perpendicular wave components
- Due to the modulation mismatch, instantaneous wave normal angles exhibit rapid variations, matching the behavior observed by spacecraft

Abstract

The chorus whistler-mode emission, a major driver of radiation belt electron energization and precipitation, exhibits significant amplitude modulations on millisecond timescales. These subpacket modulations are accompanied by fast changes in the wave normal angle. Understanding the evolution of wave propagation properties inside chorus elements is essential for modeling nonlinear chorus-electron interactions, but the origin of these rapid changes is unclear. We propose that the variations come from propagation inside thin, field-aligned cold plasma enhancements (density ducts), which produce differing modulations in parallel and perpendicular wave magnetic field components. We show that a full-wave simulation on a filamented density background predicts wave vector and amplitude evolution similar to Van Allen Probes spacecraft observations. We further demonstrate that the commonly assumed wide density ducts, in which wave propagation can be studied with ray tracing methods, cannot explain the observed behavior. This indirectly proves the existence of wavelength-scale field-aligned density fluctuations.

Plain Language Summary

The evolution of the Earth's outer radiation belt on short timescales is largely determined by interactions of particles with high-amplitude electromagnetic waves. One type of these electromagnetic emissions, the whistler-mode chorus, exhibits substantial variations in amplitude and propagation direction on the scale of milliseconds. Such rapid changes influence the interaction between the wave and resonant electrons. It is known that the global propagation properties of chorus can be explained by assuming the presence of increases and decreases in plasma density stretched along magnetic field lines (so-called density ducts). We assume the existence of wavelength-scale density ducts and compare two-dimensional solutions of wave equations with chorus signals detected by the Van Allen Probes spacecraft. We demonstrate that, unlike wide ducts, the small-scale irregularities can well explain the observed local wave propagation properties. Our simulations thus indirectly prove the existence of small-scale density fluctuations, which should be accounted for in the analysis of the fine structure of all magnetospheric whistler wave signals.

1 Introduction

The whistler-mode chorus emission (Tsurutani & Smith, 1974; Sazhin & Hayakawa, 1992) is a significant driver of acceleration and scattering of energetic electrons in the Earth’s outer radiation belt (Horne et al., 2003; Summers et al., 2007; Lam et al., 2010; Foster et al., 2017). It appears in time-frequency spectrograms as a train of narrowband chirping elements, with each element lasting for hundreds of milliseconds. The power spectrum is often divided by a gap into the lower band, $0.1\Omega_{e0}$ to $0.5\Omega_{e0}$ (where Ω_{e0} is the equatorial electron gyrofrequency), and the upper band, $0.5\Omega_{e0}$ to $0.8\Omega_{e0}$ (Tsurutani & Smith, 1974; Gao et al., 2019).

Here we focus on the lower-band chorus with a positive chirp rate, the so-called risers. Spacecraft observations have revealed subpacket modulations inside high-amplitude risers (Santolík, Gurnett, et al., 2003), accompanied by irregularities in the instantaneous frequency and the wave vector direction (Santolík et al., 2014). Several simulation studies (Hiraga & Omura, 2020; Zhang et al., 2020; Foster et al., 2021; Hanzelka et al., 2021) have shown that the subpacket structure and fine features of the wave phase evolution influence the efficiency of nonlinear wave-particle interactions. However, there is no consensus on the origin of subpackets, with current models providing only partial explanations (Hanzelka et al., 2020; Tsurutani et al., 2020; Zhang et al., 2020; Tao et al., 2021).

A common aspect of the above-mentioned models is a one-dimensional propagation along magnetic field lines on a smooth cold plasma background. Effects of cold plasma density ducts on the propagation of constant frequency whistler waves have been studied numerically by Streltsov and Bengtson (2020) and Williams and Streltsov (2021) in a homogeneous magnetic field, showing that narrow ducts can lead to the formation of subpackets. Zudin et al. (2019) studied theoretically and numerically the effects of multiple thin ducts on ionospheric whistler waves and discovered that the ducted waves have different dispersive properties than the unducted whistler mode.

Following the results of Hanzelka and Santolík (2019) and Hosseini et al. (2021) on whistler wave propagation in thin, field-aligned density enhancements and lentil-shaped cold plasma irregularities, we propose that the peculiarities of the chorus fine structure come from the dispersion of subpackets in wavelength-scale field-aligned density filaments. We conduct two-dimensional (2D) finite-difference time-domain simulations of a rising-tone chorus propagating in a cold plasma fluid in a dipole magnetic field (Section 2) and

76 study the evolution of wave normal angle θ_k and azimuthal angle ϕ_k near the equato-
 77 rial source of parallel waves. The analysis of unducted propagation and effects of both
 78 wide and narrow density ducts on magnetic field waveforms (Sections 3.1–3.3), in com-
 79 parison to Van Allen Probe spacecraft measurements (Section 3.4), lead us to the con-
 80 clusion that the presence of wavelength-scale density variations is necessary to explain
 81 the behavior of wave propagation properties within chorus elements. The impact of these
 82 findings on the interpretation of in-situ whistler-mode measurements is discussed in Sec-
 83 tion 4.

84 2 Methods

85 2.1 Wave Simulations

86 We study the propagation of whistler-mode waves by solving Maxwell’s curl equa-
 87 tions together with the equations of motion for a cold electron fluid. For our purposes,
 88 the linearized fluid motion is sufficient, and after converting velocities to current den-
 89 sities, the equations read

$$\nabla \times \mathbf{B}_w = \mu_0 \mathbf{J} + \frac{1}{c^2} \frac{\partial \mathbf{E}_w}{\partial t}, \quad (1)$$

$$\nabla \times \mathbf{E}_w = -\frac{\partial \mathbf{B}_w}{\partial t}, \quad (2)$$

$$\frac{\partial(\mu_0 \mathbf{J})}{\partial t} = \frac{\omega_{pe}^2}{c^2} \mathbf{E}_w - \mu_0 \mathbf{J} \times \frac{e \mathbf{B}_0}{m}. \quad (3)$$

90 The following quantities and notation were used: speed of light c , elementary charge e ,
 91 electron mass m , vacuum permeability μ_0 , time t , electron plasma frequency ω_{pe} , elec-
 92 tron current density \mathbf{J} , ambient magnetic field \mathbf{B}_0 , wave magnetic field \mathbf{B}_w ($|\mathbf{B}_w| \ll |\mathbf{B}_0|$),
 93 and wave electric field \mathbf{E}_w . In all simulation results presented in Section 3, we assume
 94 a perfect dipole field \mathbf{B}_0 with the strength of $30 \mu\text{T}$ at $x = 1R_E$, $z = 0$. Here, R_E stands
 95 for the Earth’s radius, and (x, z) are the solar magnetic (SM) coordinates.

96 The set of Equations 1-3 is solved by finite difference methods on a 2D staggered
 97 Yee grid, a standard approach described, e.g., in Taflove and Hagness (2005). Some re-
 98 cent examples of the application of the FDTD (finite-difference time-domain) method
 99 in whistler wave simulations can be found in Katoh (2014) and Hosseini et al. (2021).
 100 In our implementation, the simulation box spans from $-30c\Omega_{e0}^{-1}$ to $350c\Omega_{e0}^{-1}$ in the z -
 101 direction and $x_0 - 50c\Omega_{e0}^{-1}$ to $x_0 + 40c\Omega_{e0}^{-1}$ in the x -direction, where $x_0 = 5.6R_E$ is the
 102 center of the wave source at $z = 0$. Absorption coefficients are applied to each side of

103 the box to prevent interference with reflected waves. For additional details on the grid
 104 parametrization and time stepping, see Text S1 in the Supporting Information (SI).

105 The chorus element is generated by a cold current source $\mathbf{J}_s(t, x)$ at the equator,
 106 defined as

$$\mathbf{J}_s(t, x) = \mathbf{J}_0(t) \cos^2\left(\frac{\pi(x-x_0)}{2w_J}\right) \quad \text{for } |x - x_0| \leq w_J, \quad (4)$$

$$\mathbf{J}_s(t, x) = 0 \quad \text{for } |x - x_0| > w_J, \quad (5)$$

107 where w_J stands for the halfwidth of the source. Based on the analysis of transverse di-
 108 mensions of chorus by Santolík and Gurnett (2003), we set $w_J = 150$ km. The time-
 109 dependent quantity $\mathbf{J}_0(t)$ defines the whistler-mode wave properties:

$$\mathbf{J}_0(t) = J_0 A(t) (\cos(\varphi(t)), \sin(\varphi(t)), 0) \quad \text{for } t \in [0, t_{\max}]. \quad (6)$$

110 The z -component of \mathbf{J}_0 is explicitly set to zero to model a source of parallel whistler waves.
 111 The frequency grows linearly in time with $\omega_0 = \partial\varphi/\partial t(0) = 0.15\Omega_{e0}$ and $\omega_1 = \partial\varphi/\partial t(t_{\max}) =$
 112 $0.5\Omega_{e0}$, $t_{\max} = 4000\Omega_{e0}^{-1}$. $A(t)$ defines the subpacket modulations, corresponding in our
 113 simplified case to 10 subpackets of equal duration from $t = 0$ to $t = t_{\max}$, each of them
 114 modeled by a $\cos^2(t)$ function. $A(t)$ also defines the ramp-up and fade-out phase of the
 115 current, each take $t_{\text{ramp}} = t_{\max}/8$ and are also modeled by a $\cos^2(t)$ function. We keep
 116 the amplitude J_0 constant for simplicity; its exact value is unimportant since the equa-
 117 tions of motion are linearized and thus do not exhibit nonlinear effects at large wave am-
 118 plitudes.

119 The propagation of the modulated whistler-mode wave defined above is studied on
 120 three different cold plasma density backgrounds. In the unducted case, we choose a con-
 121 stant density, corresponding to $\omega_{pe0} = 5\Omega_{e0}$. In the second case, we investigate the ef-
 122 fects of a wide, strong duct, and in the third case, we look at wave propagation in many
 123 thin, weak ducts. All ducts have Gaussian profiles and are implemented as

$$n_e = n_{e0} \left(1 - \sum_{i=0}^{N_d} \delta n_i \left(1 - e^{-\frac{(L - L_{di})^2}{2\sigma_{Li}}} \right) \right), \quad (7)$$

124 where N_d is the number of ducts, δn is the relative density change, L_d is the central field
 125 line, and σ_L is the characteristic width of a duct characterized by the standard devia-
 126 tion, with subscript i serving as a duct index. The wide duct is modeled with $N_d = 1$,
 127 $\delta n = 0.1$, $L_d = 5.6$ and $\sigma_L = 0.0235$ (~ 150 km at the equator). The thin ducts have
 128 a smaller relative density increase and width, $\delta n = 0.03$ and $\sigma_L = 0.00228$ (~ 15 km

129 at the equator), and the centers of adjacent ducts are spaced by $4\sigma_L$; we use $N_d = 19$
 130 thin ducts. Notice that due to the two-dimensionality of our model, the ducts are effec-
 131 tively slabs and not tubes, as they have no dependence on the y -coordinate.

132 According to the ray tracing results of Hanzelka and Santolík (2019), the density
 133 gradients resulting from our choices of δn and σ_L should be large enough to guide lower-
 134 band whistler waves, but note that the characteristic width of 15 km for thin ducts is com-
 135 parable to equatorial wavelengths (22 km for $\omega = 0.25\Omega_{e0}$ and $\theta_k = 0^\circ$), making the
 136 approximations of ray optics invalid. This approximation is clearly still valid for the wide
 137 duct, which is by one order of magnitude larger. We also conducted numerical tests to
 138 confirm that the series of thin ducts is above the threshold discovered by Zudin et al.
 139 (2019), under which a comb of narrow density enhancements can be effectively replaced
 140 by a smoothed density profile.

141 The 2D density distributions for the set of thin ducts and for the wide duct are il-
 142 lustrated in Figures S1 and S2 in the Supporting Information, together with examples
 143 of simulated spatial distributions of the B_x and B_z components. For comparison, Fig-
 144 ure S3 shows an example of these spatial distributions for a case with a homogeneous
 145 plasma density without any ducts.

146 2.2 Signal Analysis

147 In each simulation, probes were placed inside the box to record time series of the
 148 three magnetic field components B_x , B_y , B_z . The position of these probes was defined
 149 by a series of magnetic latitudes going from 0.25° to 4.75° with a step of 0.75° , and a
 150 series of L-values going from $5.6 - 2\sigma_L$ to $5.6 + 2\sigma_L$ with a step of σ_L (35 probes in to-
 151 tal). In the unducted case, σ_L defaults to $1c\Omega_{e0}^{-1}$ at the magnetic equator. Considering
 152 the relatively low velocities of Earth orbiters like the Van Allen Probes (RBSP), whose
 153 data are later used for comparison (Section 3.4), the simulation probes were kept sta-
 154 tionary. The recorded waveforms of perpendicular and parallel magnetic field compo-
 155 nents are the primary data product of our simulations.

156 The time series of the three magnetic field components B_x , B_y , B_z , obtained ei-
 157 ther from the simulation probes or Van Allen Probes, are first rotated to the field-line
 158 coordinate system and then transformed into analytic signals with the Hilbert transform.
 159 The magnitude of the analytic signal represents the envelope of each waveform. The in-

stantaneous wave frequency is computed as a numerical derivative (forward difference) of the phase of the signal. In the experimental data, a band-pass filter $0.1\Omega_{e0} < \omega < 0.49\Omega_{e0}$ is applied before the transform, and we use the Savitzky-Golay filter to obtain the derivative of phase.

A normalized wave vector $\boldsymbol{\kappa}$ is calculated by the singular value decomposition (SVD) methods described by Santolík, Parrot, and Lefeuvre (2003). The wave normal angle and azimuthal angle are defined as

$$\theta_{\mathbf{k}} = \arctan2(\sqrt{\kappa_{x'}^2 + \kappa_{y'}^2}, \kappa_{z'}), \quad (8)$$

$$\phi_{\mathbf{k}} = \arctan2(\kappa_{y'}, \kappa_{x'}), \quad (9)$$

where the primed coordinates signify the field-aligned system (z' points along the local field line, y' points eastward, and x' completes an orthogonal, right-handed system). Under this definition, $\phi_{\mathbf{k}} = 0^\circ$ means outward propagation, and $\theta_{\mathbf{k}}$ is always positive.

3 Results

3.1 Unducted Propagation

In the unducted case, we choose the probe at $\lambda_m = 2.5^\circ$, $L = 5.6 - 2\sigma_L$, which corresponds to $\bar{x} = -12.20c\Omega_{e0}^{-1}$, $z = 155.58c\Omega_{e0}^{-1}$, where we defined $\bar{x} \equiv x - x_0$. The simulation runs with the wave and background parameters given in Section 2.1 and stops when the last subpacket reaches box boundaries.

In Figures 1a-b, we present the $B_{x'}$, $B_{z'}$ magnetic waveforms recorded by the probe. The increase in amplitude with each subpacket is caused partially by the constant value of J_0 across all frequencies but primarily by the decreasing angle between \mathbf{B}_0 and the group velocity, leading to different propagation paths for each packet (note that the first and the last subpacket are strongly affected by the ramp-up of the current). Another dispersion effect is seen at frequencies above $\Omega_e/4$, where the group velocity of a subpacket is larger than the group velocity of the following one. As a result, packets start overlapping, pulling the local minima up to nonzero values – this is best seen on the amplitude envelopes in Figure 1c.

The instantaneous frequency (Figure 1d) exhibits a linear trend, with almost no difference between the perpendicular and the parallel waveform components. Between adjacent subpackets, small ripples appear, with short intervals of negative chirp rates.

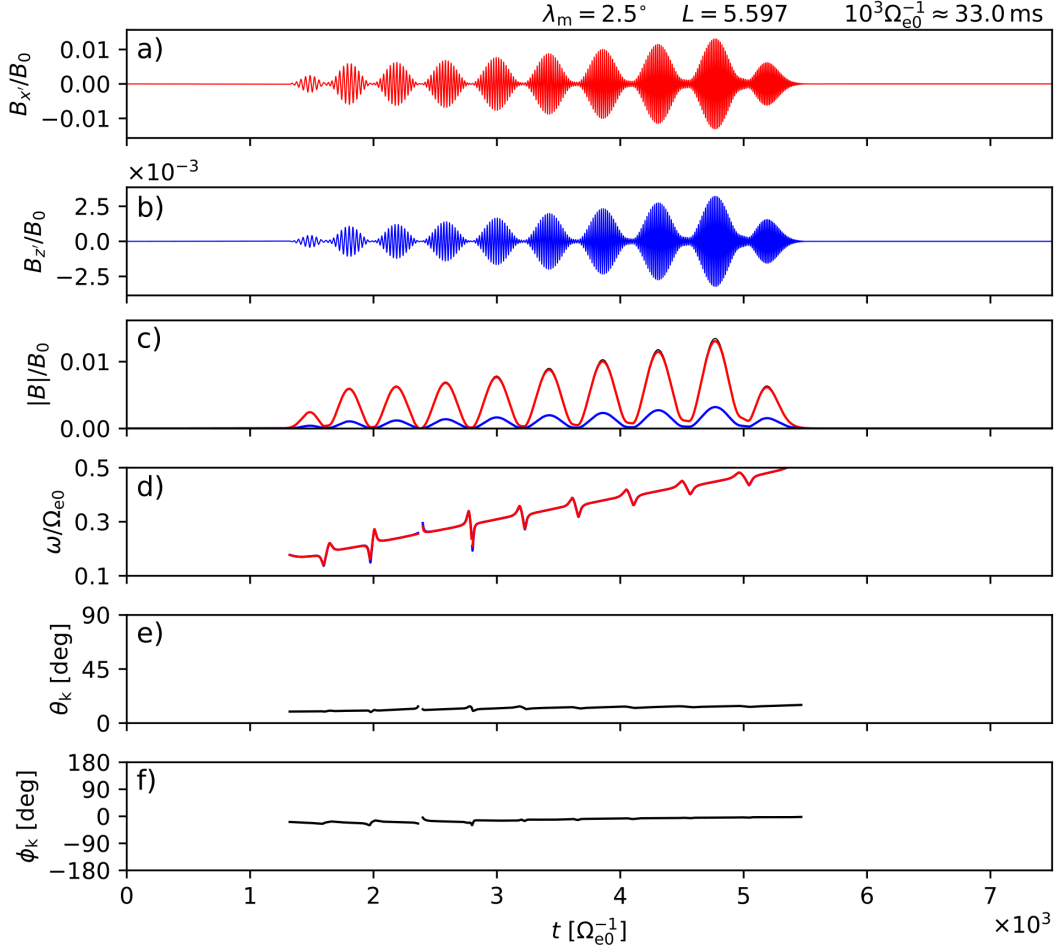


Figure 1. Simulated unducted propagation of a lower-band chorus riser with a subpacket structure. a,b) Waveforms of the perpendicular (red) and parallel (blue) magnetic field components recorded by a probe positioned at $\lambda_m = 2.5^\circ$, $L = 5.597$. c) Amplitude envelopes of the two components from previous panels (red and blue lines) and the total magnetic field (black line). d) Instantaneous frequency obtained from the analytic signal. e) Wave normal angle computed with SVD methods. f) Azimuthal angle of the wave vector, obtained with SVD methods. In panels d-f), intervals corresponding to amplitudes below 1% of the maximum are not plotted.

188 These irregularities look similar to those in the Hanzelka et al. (2020) model of chorus
 189 risers, but here, they come from amplitude modulations instead of inherent nonlinear fre-
 190 quency variations in the source. The explanation for this effect can be found through
 191 the second-order expansion of the dispersion relation $\omega(\mathbf{k})$ around the average wavenum-
 192 ber (Wait, 1965), which reveals that short pulses will experience significant spreading
 193 in the time domain during propagation in dispersive media. As a result, the edges of ini-
 194 tially separate packets start overlapping, leading to phase jumps and associated frequency
 195 irregularities. Notice that for $\omega < \Omega_e/4$, the frequency ripple has an down-up-down form,
 196 and for $\omega > \Omega_e/4$, it changes to up-down-up. This is because for quasiparallel whistler
 197 waves, the derivative of V_g with respect to ω changes its sign at $\Omega_e/4$. These features
 198 could change if the phase discontinuities were already present in the source, as in one
 199 of the models studied by Zhang et al. (2020).

200 Another deviation from the constant positive chirp rate can be found inside the first
 201 subpacket, which appears to have a nearly constant frequency. This is again a second-
 202 order propagation effect, which causes chirping of short pulses in dispersive media. Whistler
 203 pulses with $\omega > \Omega_e/4$ gain a positive chirp, which combines with the frequency growth
 204 present in the source. For $\omega < \Omega_e/4$, we get a negative chirp rate, which explains the
 205 suppression of frequency growth at the beginning of the chorus element.

206 The wave normal angle in Figure 1e rises from 10° to 18° , with negligible fluctu-
 207 ations near the amplitude minima. These values are consistent with our knowledge about
 208 the unducted propagation of whistler waves (Breuillard et al., 2012; Hanzelka & Santolík,
 209 2019). The azimuthal angle ϕ_k (Figure 1f) deviates from the outward direction by less
 210 than 30° across all frequencies. Overall, the propagation properties of unducted chorus
 211 subpackets do not exhibit any unexpected behavior.

212 3.2 A Single Wide Duct

213 The second simulation shows the propagation of a chorus element in a single duct
 214 with a large width and density variation ($\sigma_L = 0.0235$, $\delta n = 0.1$). The probe is placed
 215 at $\lambda_m = 3.25^\circ$, $L = 5.6$ (i.e., exactly at the central field line), which corresponds to
 216 $\bar{x} = -17.23c\Omega_{e0}^{-1}$ and $z = 202.06c\Omega_{e0}^{-1}$. The latitudinal placement was changed from
 217 the unducted scenario in Section 3.1 to show some of the behavior related to wave fo-

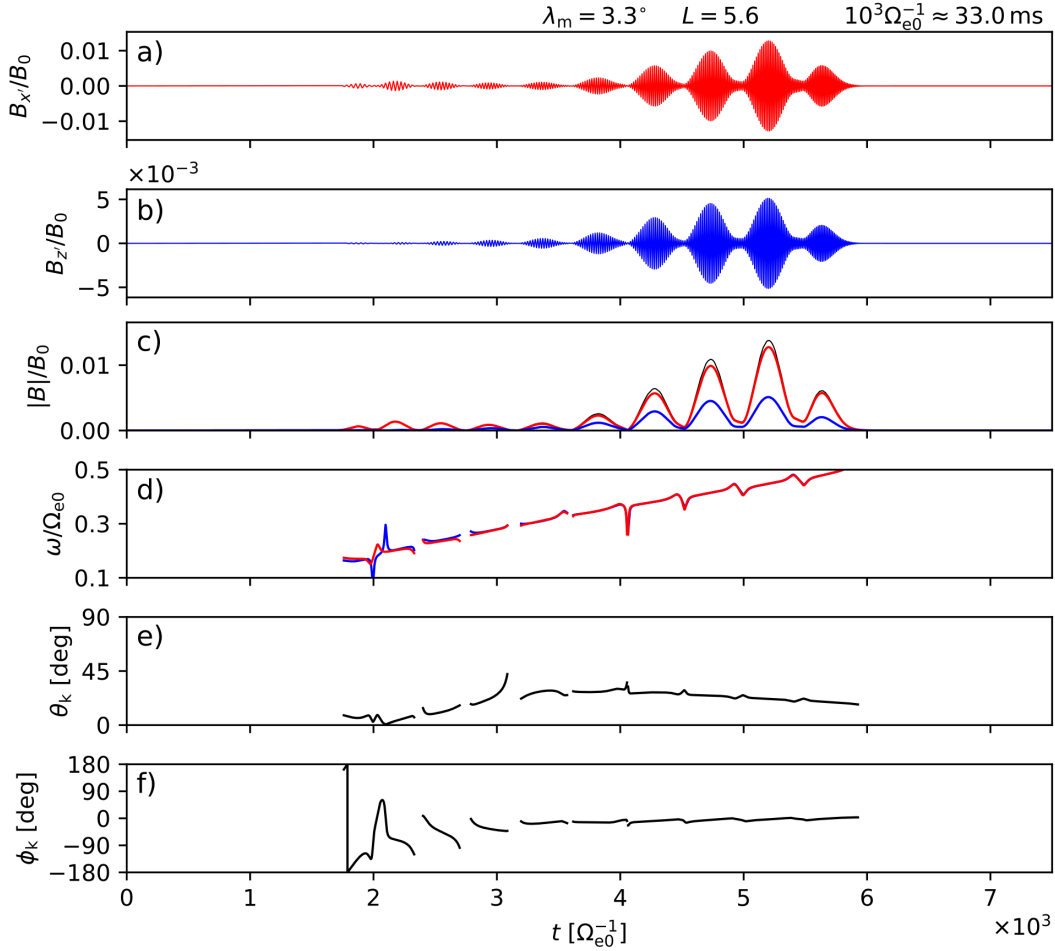


Figure 2. Simulated ducted propagation of a lower-band chorus riser with a subpacket structure. The panel format is the same as in Figure 1. The probe was placed at $\lambda_m = 3.25^\circ$ and $L = 5.6$.

218 cussation in ducts – see Figure S2 in the SI for placement of the probe within a wavefield
 219 snapshot.

220 Figure 2 shows the waveforms and wave properties in the same format as Figure
 221 1. Because the packets are now focused by the duct and each frequency reflects at a dif-
 222 ferent distance from the central field line, the low-frequency part of the element appears
 223 to have amplitudes about an order of magnitude smaller than the maximum. As in the
 224 unducted case, higher frequency packets exhibit slight overlaps. The amplitude modu-
 225 lation of the two waveforms is slightly mismatched at the beginning of the element, which
 226 manifests in the different frequency behavior of each component in the first two subpack-
 227 ets (Fig. 2c-d).

Another consequence of the $B_{x'}-B_{z'}$ envelope mismatch is the larger variations in wave normal angle (Fig. 2e); nevertheless, there is a clear rising trend, followed by a gradual decrease. The azimuthal angles (Fig. 2f) vary wildly in the weaker, low-frequency portion of the element, switching from outward to inward propagation. As the element evolves, the values of ϕ_k converge to zero degrees.

3.3 Multiple Thin Ducts

The third and last simulation follows the propagation of a chorus element in a comb of weak and narrow ducts ($\delta n = 0.03$, $\sigma_L = 0.00228$). The probe is positioned at $\lambda_m = 2.5^\circ$, $L = 5.6 + 2\sigma_L$, corresponding to $\bar{x} = -7.31c\Omega_{e0}^{-1}$ and $z = 155.80c\Omega_{e0}^{-1}$.

The perpendicular and parallel magnetic field waveforms in Figures 3a-b now differ significantly, especially towards higher frequencies, where additional subpackets appear. This is partially due to the group velocity dispersion, as already discussed in the unducted case, but also due to the spatial variation of amplitude caused by splitting of subpackets by the density filaments (compare with Figure S1). The total magnetic field in Figure 3c starts to oscillate toward the end of the element, suggesting a significant deviation from circular polarization. As in the case of a single duct, the frequencies of $B_{x'}$ and $B_{z'}$ (Fig. 3d) do not exactly match, especially in the time intervals around amplitude minima.

The evolution of wave normal angle in Figure 3e shows rapid variations from 0° up to about 60° , with no clear trend to the average $\theta_k(t)$ across the element. The prominent peaks in θ_k appear when the amplitude of $B_{x'}$ reaches a local minimum of a deep modulation, while the amplitude of $B_{z'}$ stays far away from its local minima. These differences in amplitude modulation of perpendicular and parallel components are apparent towards higher frequencies – the last three pairs of amplitude minima are highlighted in Figure 3 by vertical lines. Similar to θ_k , we observe large variations in the azimuthal angle ϕ_k , with the outward propagation direction being dominant in the recorded waveform.

3.4 Comparison with Spacecraft Observations

The propagation characteristics retrieved from full-wave simulations are compared to Van Allen Probes observations. As a representative example, we chose a lower-band

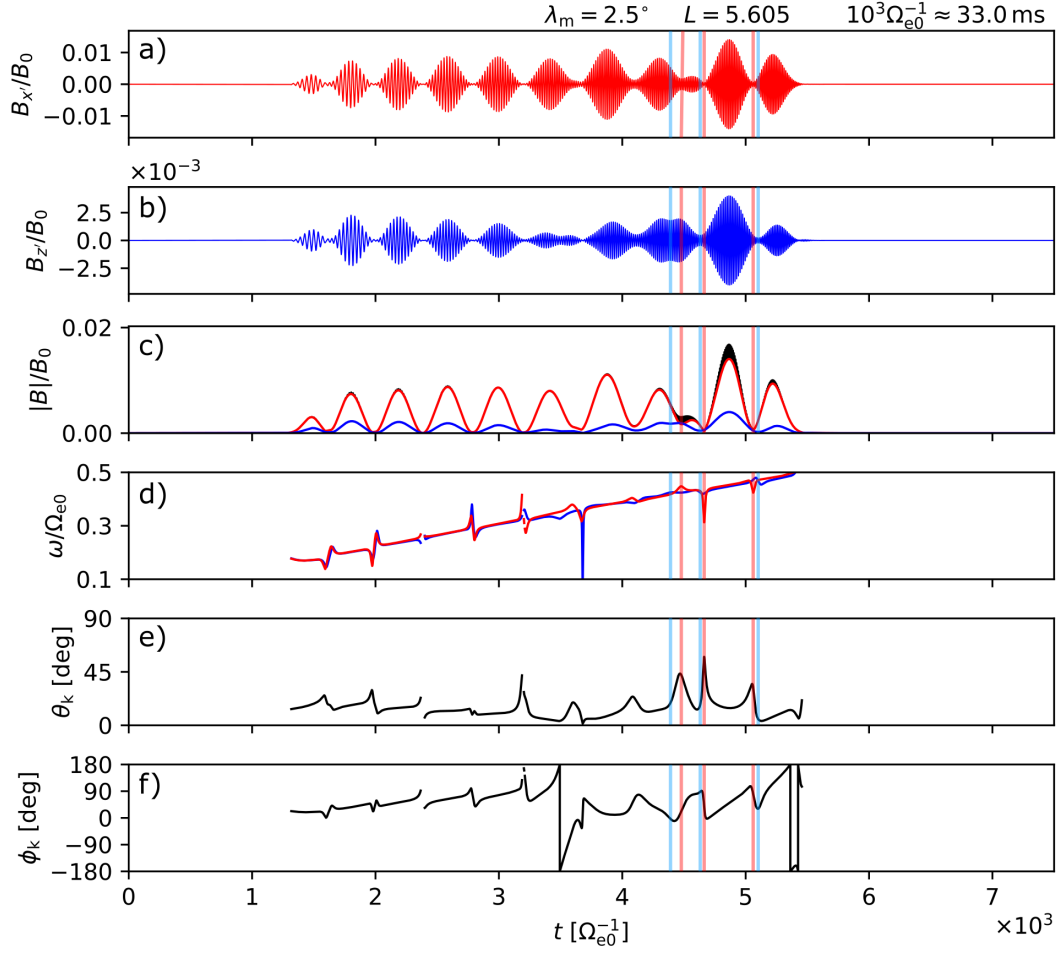


Figure 3. Simulated propagation of a lower-band chorus riser with a subpacket structure on a cold plasma density background modulated by a series of thin ducts. The panel format is the same as in Figure 1, with the addition of red and blue vertical lines, which highlight the amplitude minima of the last three subpackets in the perpendicular and parallel waveforms. The probe was placed at $\lambda_m = 2.5^\circ$ and $L = 5.605$.

258 riser observed on 20 November 2012 at 12:05:29.74 UT – 12:05:29.94 UT by the EMFI-
 259 SIS instrument of Probe A. The spacecraft was located at $L = 5.78$, -1.1° of magnetic
 260 dipole latitude. The plasma-to-cyclotron frequency ratio was measured to be $\omega_{pe}/\Omega_e =$
 261 5.14, based on fluxgate data and upper hybrid resonance detection on EMFISIS (Kurth
 262 et al., 2015). The frequency of the element ranged from about $0.26\Omega_e$ to $0.47\Omega_e$. The
 263 waveforms were recorded with 35 kHz sampling and processed according to Section 2.2.
 264 A Savitzky-Golay filter of 3rd order with a window length of 101 points was applied to
 265 the amplitude and phase of analytic signals $B_{x'}$ and $B_{z'}$, and the filtered data were then
 266 used to obtain the wave properties. The final products are displayed in Figure 4 in the
 267 same format as for the simulation results in Figures 1-3.

268 Looking at $B_{x'}$ and $B_{z'}$ waveforms in Figures 4a-b from $t = 4.095$ s onward, we
 269 observe that the subpacket structure matches at lower frequencies, but discrepancies ap-
 270 pear as the element evolves. The amplitude modulations also become less regular, with
 271 alternating shorter and longer subpackets – this corresponds well to the simulation with
 272 many thin ducts. Furthermore, oscillations of the total field (loss of circular polariza-
 273 tion) appear in Figure 4c, which is again a feature observed in simulation only when wavelenth-
 274 scale ducts are present.

275 The frequency (Fig. 4d) follows a positive linear trend up to about $0.43\Omega_e$ (1.6 kHz),
 276 where the growth slows down. The discontinuities between adjacent subpackets have a
 277 different character from those in simulations (for $\omega > 0.25\Omega_e$): the up-down-up ripple
 278 is replaced by a simpler up-down form, which ends at a higher frequency value than it
 279 started. This behavior might come from the more shallow modulations in the experimen-
 280 tal data, or it could be related to the apparent lack of chirp inside the subpackets – com-
 281 pare this to the subpacket chirp rate analysis by (Tsurutani et al., 2020). The frequency
 282 growth pattern falls apart as the subpacket structure becomes more complex. During
 283 the evolution, the mismatch between instantaneous frequencies of $B_{x'}$ and $B_{z'}$ becomes
 284 stronger.

285 The wave normal angle (Fig. 4e) exhibits rapid variations with jumps up to about
 286 60° , which agrees with the duct-induced patterns displayed in Figure 3e. Based on the
 287 behavior of the azimuthal angle in Figure 4f, the propagation direction switches from out-
 288 ward to inward more often than in simulations, especially in the high-frequency part of
 289 the element. However, comparing the azimuthal behavior with simulations may be in-

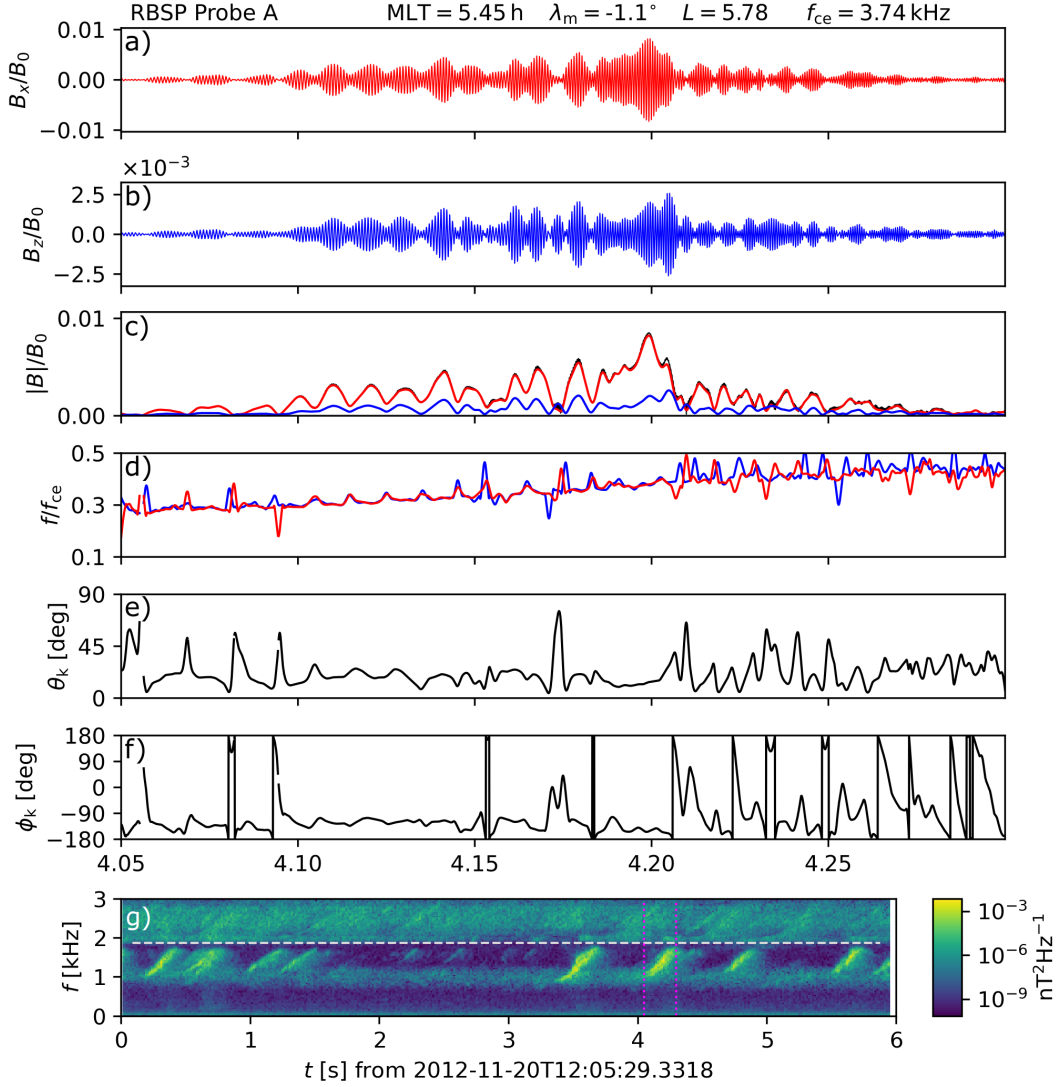


Figure 4. Rising-tone chorus observation made by the EMFISIS instrument on Van Allen Probe A. Panels a-f) show the same type of data as the simulation results in Figure 1, with Savitzky-Golay filter applied on $B_{x'}$ and $B_{z'}$ before processing data for panels d) to f). Panel g) shows an unfiltered spectrogram constructed from a 6-second burst mode snapshot, with the chosen element delimited by dotted magenta lines. The white dashed line represents one half of the gyrofrequency. In panels d-f), intervals corresponding to amplitudes below 1% of the maximum are not plotted.

290 appropriate, because ducts in the 2D simulation are slab-like structure, unbounded in
 291 longitude, while the real ducts are expected to be cylindrical, which was proven in iono-
 292 spheric environment by Loi et al. (2015). Difference in dispersive properties of 2D and
 293 3D ducted whistler modes was shown theoretically by Zudin et al. (2019).

294 Overall, we conclude that the experimentally observed patterns in subpacket mod-
 295 ulations and wave propagation properties are best explained by the presence of many
 296 thin ducts as opposed to a single wide duct or unducted propagation.

297 4 Discussion and Conclusion

298 The waveforms shown in Section 3 were recorded at a few fixed points in space, cho-
 299 sen to be about 1500–2000 km from the equatorial source. However, the chorus emissions
 300 have a drifting source that can move thousands of kilometers upstream within a single
 301 element (Santolík et al., 2004; Demekhov, Taubenschuss, et al., 2020; Nogi & Omura,
 302 2022). It is therefore difficult to estimate how far from the source did Van Allen Probes
 303 detect the emission, and how much the waveform could have been affected by propaga-
 304 tion effects. Presumably, the high-frequency tail of a chorus element should be affected
 305 by propagation more strongly, which is corroborated by the case presented in Figure 4.
 306 Comparing simulations to in-situ data obtained too close to the source should be avoided
 307 because of the overlap of counter-streaming elements, unless we manage to separate them
 308 with an empirical mode decomposition method like the Hilbert-Huang transform (Huang
 309 & Wu, 2008). Another caveat is the determination of wave propagation properties near
 310 amplitude minima. In our example from Figure 4, peaks in θ_k typically appear when the
 311 total amplitude is significant, but in a general case, the narrow hiss band from which the
 312 spectral elements grow could interfere with the propagation analysis.

313 According to our thin-duct propagation hypothesis, the subpacket modulations and
 314 θ_k and ϕ_k behavior should become less regular as we go further from the source, espe-
 315 cially at higher frequencies. That the few first subpackets can be more regular has al-
 316 ready been shown by Santolík, Gurnett, et al. (2003), Crabtree et al. (2017) and Foster
 317 et al. (2021), but a statistical analysis is needed. Additionally, the thin duct structure
 318 will cause varying amplitude modulations when measuring at multiple points at a fixed
 319 latitude but different field lines – Figures S4 and S5 in the Supporting Information show
 320 that a few tens of kilometers are enough to completely change the subpacket structure.

321 This behavior agrees with the multipoint Cluster spacecraft observations of Santolík, Gur-
322 nett, et al. (2003) but needs to be confirmed by a more extensive analysis, both numer-
323 ical and experimental.

324 An interesting but not surprising feature of the waveforms from Figure 3 are the
325 2ω -oscillations of the total magnetic field, corresponding to elongation of the polariza-
326 tion ellipse. According to the homogeneous cold plasma dispersion relation (Stix, 1992),
327 the ratio of semi-major to semi-minor axis in the lower frequency band of chorus should
328 not deviate from unity by more than about 1%. However, our plasma is strongly inho-
329 mogenous, and the well-known dispersion relation for whistler waves cannot be applied.
330 The detection of similar magnetic field oscillations by Van Allen Probes (Fig. 4c here
331 and Fig. 3c in Santolík et al. (2014)) is another piece of evidence supporting our thin-
332 duct hypothesis and will be analyzed in more detail in our future investigations.

333 A natural question following our propagation analysis concerns with the origin of
334 the assumed density filamentations. According to the simplified calculations presented
335 by Weibel (1977), the ponderomotive force of high-amplitude whistler waves should have
336 a radial component that forces electrons to move up the amplitude gradient, creating thus
337 the hypothesized ducts. Laboratory experiments by Stenzel (1976) and their theoret-
338 ical analysis by Sodha and Tripathi (1977) corroborate the tendency of strong whistler
339 waves to self-focus through the formation of density filaments. A more advanced the-
340 oretical model of self-channeling and amplitude modulation based on the nonlinear Schrödinger
341 equation was developed by Eliasson and Shukla (2004). However, as far as we know, there
342 has been no first-principle numerical study confirming this behavior, and the expected
343 density modulations are too weak and narrow to be detected in-situ by spacecraft. The
344 results of Yearby et al. (2011) obtained from the Cluster spacecraft potential show lo-
345 calized density enhancements and depletion, but the presence of strong whistler waves
346 puts the validity of the potential method into question.

347 Finally, we must emphasize that wide ducts (as the one assumed in Section 3.2)
348 are undoubtedly present in the inner magnetosphere and play a major role in the global
349 properties of whistler waves (Demekhov, Titova, et al., 2020; Artemyev et al., 2021; Chen
350 et al., 2021). However, when inspecting the fine structure of chorus, we need to consider
351 the presence of narrow ducts as well, as they provide a simple and convincing explana-
352 tion for the behavior of wave propagation properties and amplitude modulations on mil-

353 lisecond timescales. Effects of such density irregularities might be difficult to separate
 354 from nonlinear growth effects predicted by one-dimensional chorus theories (Tao et al.,
 355 2020; Omura, 2021; Zonca et al., 2021). This difficulty cannot be overcome even with
 356 2D PIC simulation (e.g., Ke et al. (2017)) because they treat consistently only the hot
 357 electrons and not the cold population. These limitations should be kept in mind dur-
 358 ing any future attempts to explain the subpacket structure of chorus with nonlinear growth
 359 theories.

360 5 Open Research

361 The Van Allen Probe data are publicly available from the NASA's Space Physics
 362 Data Facility, repository <https://spdf.gsfc.nasa.gov/pub/data/rbsp/>. The FDTD
 363 simulation Python code, resulting time series data and processing and plotting routines
 364 can be downloaded from <https://doi.org/10.6084/m9.figshare.20319063>.

365 Acknowledgments

366 This work has received funding from the European Union's Horizon 2020 research and
 367 innovation programme under grant agreement No. 870452 (PAGER).

368 References

- 369 Artemyev, A. V., Demekhov, A. G., Zhang, X. J., Angelopoulos, V., Mourenas, D.,
 370 Fedorenko, Y. V., ... Shinohara, I. (2021, November). Role of Ducting in
 371 Relativistic Electron Loss by Whistler-Mode Wave Scattering. *J. Geophys.*
 372 *Res. Space Physics*, 126(11), e29851. doi: 10.1029/2021JA029851
- 373 Breuillard, H., Zaliznyak, Y., Krasnoselskikh, V., Agapitov, O., Artemyev, A., &
 374 Rolland, G. (2012, August). Chorus wave-normal statistics in the Earth's
 375 radiation belts from ray tracing technique. *Ann. Geophys.*, 30(8), 1223-1233.
 376 doi: 10.5194/angeo-30-1223-2012
- 377 Chen, R., Gao, X., Lu, Q., Chen, L., Tsurutani, B. T., Li, W., ... Wang, S. (2021,
 378 April). In Situ Observations of Whistler Mode Chorus Waves Guided by Den-
 379 sity Ducts. *J. Geophys. Res. Space Physics*, 126(4), e28814. doi: 10.1029/
 380 2020JA028814
- 381 Crabtree, C., Tejero, E., Ganguli, G., Hospodarsky, G. B., & Kletzing, C. A. (2017).
 382 Bayesian spectral analysis of chorus subelements from the van allen probes. *J.*

- 383 *Geophys. Res. Space Physics*, 122(6), 6088-6106. doi: 10.1002/2016JA023547
- 384 Demekhov, A. G., Taubenschuss, U., Hanzelka, M., & Santolík, O. (2020, March).
 385 Frequency Dependence of Very Low Frequency Chorus Poynting Flux in the
 386 Source Region: THEMIS Observations and a Model. *Geophys. Res. Lett.*,
 387 47(6), e86958. doi: 10.1029/2019GL086958
- 388 Demekhov, A. G., Titova, E. E., Maninnen, J., Pasmanik, D. L., Lubchich, A. A.,
 389 Santolík, O., ... Turunen, T. (2020, May). Localization of the Source of
 390 Quasiperiodic VLF Emissions in the Magnetosphere by Using Simultaneous
 391 Ground and Space Observations: A Case Study. *J. Geophys. Res. Space*
 392 *Physics*, 125(5), e27776. doi: 10.1029/2020JA027776
- 393 Eliasson, B., & Shukla, P. K. (2004, September). Theoretical and numerical studies
 394 of density modulated whistlers. *Geophys. Res. Lett.*, 31(17), L17802. doi: 10
 395 .1029/2004GL020605
- 396 Foster, J. C., Erickson, P. J., & Omura, Y. (2021, December). Subpacket struc-
 397 ture in strong VLF chorus rising tones: characteristics and consequences
 398 for relativistic electron acceleration. *Earth Planets Space*, 73(1), 140. doi:
 399 10.1186/s40623-021-01467-4
- 400 Foster, J. C., Erickson, P. J., Omura, Y., Baker, D. N., Kletzing, C. A., & Claude-
 401 pierre, S. G. (2017, January). Van Allen Probes observations of prompt MeV
 402 radiation belt electron acceleration in nonlinear interactions with VLF chorus.
 403 *J. Geophys. Res. Space Physics*, 122(1), 324-339. doi: 10.1002/2016JA023429
- 404 Gao, X., Chen, L., Li, W., Lu, Q., & Wang, S. (2019, April). Statistical Results
 405 of the Power Gap Between Lower-Band and Upper-Band Chorus Waves. *Geo-*
 406 *phys. Res. Lett.*, 46(8), 4098-4105. doi: 10.1029/2019GL082140
- 407 Hanzelka, M., & Santolík, O. (2019, June). Effects of Ducting on Whistler Mode
 408 Chorus or Exohiss in the Outer Radiation Belt. *Geophys. Res. Lett.*, 46(11),
 409 5735-5745. doi: 10.1029/2019GL083115
- 410 Hanzelka, M., Santolík, O., Omura, Y., & Kolmašová, I. (2021, September). Measur-
 411 ability of the Nonlinear Response of Electron Distribution Function to Chorus
 412 Emissions in the Earth's Radiation Belt. *J. Geophys. Res. Space Physics*,
 413 126(9), e29624. doi: 10.1029/2021JA029624
- 414 Hanzelka, M., Santolík, O., Omura, Y., Kolmašová, I., & Kletzing, C. A. (2020, Au-
 415 gust). A Model of the Subpacket Structure of Rising Tone Chorus Emissions.

- 416 *J. Geophys. Res. Space Physics*, 125(8), e28094. doi: 10.1029/2020JA028094
- 417 Hiraga, R., & Omura, Y. (2020, February). Acceleration mechanism of radiation belt
418 electrons through interaction with multi-subpacket chorus waves. *Earth Planets
419 Space*, 72(1), 21. doi: 10.1186/s40623-020-1134-3
- 420 Horne, R. B., Glauert, S. A., & Thorne, R. M. (2003, May). Resonant diffusion of
421 radiation belt electrons by whistler-mode chorus. *Geophys. Res. Lett.*, 30(9),
422 1493. doi: 10.1029/2003GL016963
- 423 Hosseini, P., Agapitov, O., Harid, V., & Golkowski, M. (2021, March). Evidence of
424 Small Scale Plasma Irregularity Effects on Whistler Mode Chorus Propagation.
425 *Geophys. Res. Lett.*, 48(5), e92850. doi: 10.1029/2021GL092850
- 426 Huang, N. E., & Wu, Z. (2008, June). A review on Hilbert-Huang transform:
427 Method and its applications to geophysical studies. *Rev. Geophys.*, 46(2),
428 RG2006. doi: 10.1029/2007RG000228
- 429 Katoh, Y. (2014, December). A simulation study of the propagation of whistler-
430 mode chorus in the Earth's inner magnetosphere. *Earth Planets Space*, 66, 6.
431 doi: 10.1186/1880-5981-66-6
- 432 Ke, Y., Gao, X., Lu, Q., Wang, X., & Wang, S. (2017, August). Generation of
433 rising-tone chorus in a two-dimensional mirror field by using the general curvi-
434 linear PIC code. *J. Geophys. Res. Space Physics*, 122(8), 8154-8165. doi:
435 10.1002/2017JA024178
- 436 Kurth, W. S., De Pascuale, S., Faden, J. B., Kletzing, C. A., Hospodarsky, G. B.,
437 Thaller, S., & Wygant, J. R. (2015, February). Electron densities inferred from
438 plasma wave spectra obtained by the Waves instrument on Van Allen Probes.
439 *J. Geophys. Res. Space Physics*, 120, 904-914. doi: 10.1002/2014JA020857
- 440 Lam, M. M., Horne, R. B., Meredith, N. P., Glauert, S. A., Moffat-Griffin, T., &
441 Green, J. C. (2010, April). Origin of energetic electron precipitation ≥ 30 keV
442 into the atmosphere. *J. Geophys. Res. Space Physics*, 115(8), A00F08. doi:
443 10.1029/2009JA014619
- 444 Loi, S. T., Murphy, T., Cairns, I. H., Menk, F. W., Waters, C. L., Erickson, P. J.,
445 ... Williams, C. L. (2015, May). Real-time imaging of density ducts between
446 the plasmasphere and ionosphere. *Geophys. Res. Lett.*, 42, 3707-3714. doi:
447 10.1002/2015GL063699
- 448 Nogi, T., & Omura, Y. (2022, January). Nonlinear Signatures of VLF-Triggered

- 449 Emissions: A Simulation Study. *J. Geophys. Res. Space Physics*, *127*(1),
 450 e29826. doi: 10.1029/2021JA029826
- 451 Omura, Y. (2021, April). Nonlinear wave growth theory of whistler-mode chorus and
 452 hiss emissions in the magnetosphere. *Earth Planets Space*, *73*(1), 95. doi: 10
 453 .1186/s40623-021-01380-w
- 454 Santolík, O., & Gurnett, D. A. (2003, January). Transverse dimensions of
 455 chorus in the source region. *Geophys. Res. Lett.*, *30*(2), 1031. doi:
 456 10.1029/2002GL016178
- 457 Santolík, O., Gurnett, D. A., Pickett, J. S., Parrot, M., & Cornilleau-Wehrlin, N.
 458 (2003, July). Spatio-temporal structure of storm-time chorus. *J. Geophys. Res.*
 459 *Space Physics*, *108*, 1278. doi: 10.1029/2002JA009791
- 460 Santolík, O., Gurnett, D. A., Pickett, J. S., Parrot, M., & Cornilleau-Wehrlin,
 461 N. (2004, January). A microscopic and nanoscopic view of storm-time
 462 chorus on 31 March 2001. *Geophys. Res. Lett.*, *31*(2), L02801. doi:
 463 10.1029/2003GL018757
- 464 Santolík, O., Kletzing, C. A., Kurth, W. S., Hospodarsky, G. B., & Bounds, S. R.
 465 (2014, January). Fine structure of large-amplitude chorus wave packets. *Geo-*
 466 *phys. Res. Lett.*, *41*, 293-299. doi: 10.1002/2013GL058889
- 467 Santolík, O., Parrot, M., & Lefeuvre, F. (2003, February). Singular value decom-
 468 position methods for wave propagation analysis. *Radio Sci.*, *38*, 10-1. doi: 10
 469 .1029/2000RS002523
- 470 Sazhin, S., & Hayakawa, M. (1992). Magnetospheric chorus emissions: A re-
 471 view. *Planet. Space Sci.*, *40*(5), 681 - 697. doi: [https://doi.org/10.1016/
 472 0032-0633\(92\)90009-D](https://doi.org/10.1016/0032-0633(92)90009-D)
- 473 Sodha, M. S., & Tripathi, V. K. (1977, March). Steady-state self-focusing and fila-
 474 mentation of whistlers in a plasma. *J. Appl. Phys.*, *48*(3), 1078-1084. doi: 10
 475 .1063/1.323783
- 476 Stenzel, R. L. (1976, June). Filamentation instability of a large amplitude whistler
 477 wave. *Phys. Fluids*, *19*(6), 865-871. doi: 10.1063/1.861552
- 478 Stix, T. (1992). *Waves in Plasmas*. Melville NY: American Institute of Physics.
- 479 Streltsov, A. V., & Bengtson, M. T. (2020, October). Observations and Modeling of
 480 Whistler Mode Waves in the Magnetospheric Density Ducts. *J. Geophys. Res.*
 481 *Space Physics*, *125*(10), e28398. doi: 10.1029/2020JA028398

- 482 Summers, D., Ni, B., & Meredith, N. P. (2007, April). Timescales for radia-
 483 tion belt electron acceleration and loss due to resonant wave-particle inter-
 484 actions: 2. Evaluation for VLF chorus, ELF hiss, and electromagnetic ion
 485 cyclotron waves. *J. Geophys. Res. Space Physics*, *112*(A4), A04207. doi:
 486 10.1029/2006JA011993
- 487 Taflove, A., & Hagness, S. C. (2005). *Computational Electrodynamics: The Finite-*
 488 *difference Time-domain Method*. Artech House.
- 489 Tao, X., Zonca, F., & Chen, L. (2021, September). A “Trap-Release-Amplify” Model
 490 of Chorus Waves. *J. Geophys. Res. Space Physics*, *126*(9), e29585. doi: 10
 491 .1029/2021JA029585
- 492 Tao, X., Zonca, F., Chen, L., & Wu, Y. (2020, January). Theoretical and numerical
 493 studies of chorus waves: A review. *Sci. China Earth Sci.*, *63*(1), 78-92. doi: 10
 494 .1007/s11430-019-9384-6
- 495 Tsurutani, B. T., Chen, R., Gao, X., Lu, Q., Pickett, J. S., Lakhina, G. S., ...
 496 Falkowski, B. J. (2020, October). Lower-Band “Monochromatic” Chorus
 497 Riser Subelement/Wave Packet Observations. *J. Geophys. Res. Space Physics*,
 498 *125*(10), e28090. doi: 10.1029/2020JA028090
- 499 Tsurutani, B. T., & Smith, E. J. (1974, January). Postmidnight chorus: A
 500 substorm phenomenon. *J. Geophys. Res.*, *79*(1), 118-127. doi: 10.1029/
 501 JA079i001p00118
- 502 Wait, J. R. (1965). Propagation of pulses in dispersive media. *Radio Sci.*, *69*(11),
 503 1387–1401.
- 504 Weibel, E. S. (1977, April). Self channeling of whistler waves. *Phys. Lett. A*, *61*(1),
 505 37-39. doi: 10.1016/0375-9601(77)90256-0
- 506 Williams, D. D., & Streltsov, A. V. (2021, December). Determining Parameters
 507 of Whistler Waves Trapped in High-Density Ducts. *J. Geophys. Res. Space*
 508 *Physics*, *126*(12), e29228. doi: 10.1029/2021JA029228
- 509 Yearby, K. H., Balikhin, M. A., Khotyaintsev, Y. V., Walker, S. N., Krasnoselskikh,
 510 V. V., Alleyne, H. S. C. K., & Agapitov, O. (2011, September). Ducted prop-
 511 agation of chorus waves: Cluster observations. *Annales Geophysicae*, *29*(9),
 512 1629-1634. doi: 10.5194/angeo-29-1629-2011
- 513 Zhang, X. J., Agapitov, O., Artemyev, A. V., Mourenas, D., Angelopoulos, V.,
 514 Kurth, W. S., ... Hospodarsky, G. B. (2020, October). Phase Decoherence

- 515 Within Intense Chorus Wave Packets Constrains the Efficiency of Nonlinear
516 Resonant Electron Acceleration. *Geophys. Res. Lett.*, 47(20), e89807. doi:
517 10.1029/2020GL089807
- 518 Zonca, F., Tao, X., & Chen, L. (2021, December). Nonlinear dynamics and phase
519 space transport by chorus emission. *Rev. Mod. Plasma Phys.*, 5(1), 8. doi: 10
520 .1007/s41614-021-00057-x
- 521 Zudin, I. Y., Zaboronkova, T. M., Gushchin, M. E., Aidakina, N. A., Korobkov,
522 S. V., & Krafft, C. (2019, June). Whistler Waves' Propagation in Plas-
523 mas With Systems of Small-Scale Density Irregularities: Numerical Simula-
524 tions and Theory. *J. Geophys. Res. Space Physics*, 124(6), 4739-4760. doi:
525 10.1029/2019JA026637